

Hypersatellite x-ray decay of 3d hollow- K -shell atoms produced by heavy-ion impact

Y.-P. Maillard, J.-Cl. Dousse,^{*} J. Hozzowska, M. Berset, O. Mauron, and P.-A. Raboud
Department of Physics, University of Fribourg, CH-1700 Fribourg, Switzerland

M. Kavčič
J. Stefan Institute, SI-1001 Ljubljana, Slovenia

J. Rzadkiewicz
National Centre for Nuclear Research, PL-05-400 Otwock Swierk, Poland

D. Banaś
Institute of Physics, Jan Kochanowski University, PL-25406 Kielce, Poland

K. Tökési[†]
Institute for Nuclear Research, Hungarian Academy of Sciences (ATOMKI), H-4001 Debrecen, Hungary



(Received 21 March 2018; published 10 July 2018)

We report on the radiative decay of double K -shell vacancy states produced in solid Ca, V, Fe, and Cu targets by impact with about 10 MeV/amu C and Ne ions. The resulting K hypersatellite x-ray emission spectra were measured by means of high-energy-resolution spectroscopy using a von Hamos bent crystal spectrometer. The experiment was carried out at the Philips variable energy cyclotron of the Paul Scherrer Institute. From the fits of the x-ray spectra the energies, line widths, and relative intensities of the hypersatellite x-ray lines could be determined. The fitted intensities were corrected to account for the energy-dependent solid angle of the spectrometer, effective source size, target self-absorption, crystal reflectivity, and detector efficiency. The single-to-double K -shell ionization cross-section ratios were deduced from the corrected relative intensities of the hypersatellites and compared to theoretical predictions from the semiclassical approximation model using hydrogenlike and Dirac-Hartree-Fock wave functions and from classical trajectory Monte Carlo calculations.

DOI: [10.1103/PhysRevA.98.012705](https://doi.org/10.1103/PhysRevA.98.012705)

I. INTRODUCTION

The radiative decay of hollow- K -shell atoms, i.e., atoms with an empty K shell, leads to the emission of x rays that are shifted towards higher energies as compared to the parent diagram lines decaying ions with a single vacancy in the K shell. The K -shell vacancy which is not filled by the radiative transition is called the spectator vacancy because it is not directly involved in the transition. The energy shift is due to the diminution of the electron screening originating from the removal of the second $1s$ electron which leads to enhanced binding energies for the atomic levels. As the enhancement diminishes with the principal quantum number of the atomic levels, the binding energy change of the K shell is bigger than the one of outer shells, which results into a net increase of the transition energy. More generally, atomic structure calculations show that the energy shifts of x-ray lines emitted by doubly ionized atoms decrease with the principal quantum number of the shell where the spectator vacancy is located. For K x rays, the strongest energy shift is thus observed when the

spectator vacancy is located in the same shell as the initial vacancy involved in the transition, i.e., the K shell. In this case, the shift is much bigger than the one observed for L or M satellites and for this reason x rays emitted by doubly K -shell ionized atoms are named K hypersatellites.

The first theoretical investigation of the radiative decay of hollow atoms was done by Heisenberg [1] more than 90 years ago and the first experimental evidence concerning the radiative decay of hollow- K -shell atoms was reported by Charpak [2] in 1953. Charpak's approach consisted to measure in coincidence the two photons emitted sequentially by the radiative decay of hollow- K -shell ^{55}Mn atoms ($Z = 25$) resulting from the nuclear decay of ^{55}Fe ($Z = 26$), using two gas proportional counters for the coincident detection of the two photons. In this pioneering work, the double $1s$ ionization of the Mn atoms resulted directly from the nuclear decay, the first $1s$ electron being captured by the ^{55}Fe nucleus (nuclear electron capture) and the removal of the second one resulting from the shake process following the nuclear decay induced abrupt change of the atomic potential. Actually, the two x rays detected in coincidence corresponded to the cascade of a K -hypersatellite transition followed by a KL^{-1} -satellite transition but the small energy difference between these two x rays could not be distinguished by Charpak with the employed gas detectors. A similar coincidence experiment was

^{*}jean-claude.dousse@unifr.ch

[†]Also at ELI-ALPS, ELI-HU Non-Profit, Ltd., H-6720 Szeged, Hungary.

performed some years later by Briand *et al.* [3] to investigate the radiative decay of double $1s$ vacancy states in ^{71}Ga atoms ($Z = 31$) produced by the K -electron capture decay of ^{71}Ge ($Z = 32$). It is interesting to note here that in the early days of x-ray spectroscopy (XRS) the x-ray line associated to the $K^{-2}-K^{-1}L^{-1}$ transition was usually named $K\alpha_4$ satellite [4] and to our best knowledge the word $K\alpha$ hypersatellite was used for the first time in 1971 by Briand *et al.* in [5].

The probability to produce a double K -shell ionization via nuclear decay processes such as nuclear electron capture, β decay, or α decay is very weak, typically in the order of 10^{-4} . The same holds for the excitation of the sample with photons, double K -shell photoionization (DPI) probabilities varying between 10^{-2} for light elements down to 10^{-6} for high- Z elements as a consequence of the approximate Z^{-4} dependence of the DPI cross section. In the DPI process, the second $1s$ electron is removed as a result of a shake [6,7] or knockout (KO) process [8]. The shake process is a quantum mechanics effect in which a bound electron can be ionized [shakeoff (SO) process] or promoted into an unfilled outer subshell [shakeup (SU) process]) as a consequence of the sudden change of the atomic potential following the photoabsorption. In the KO mechanism which can be regarded as an inelastic electron-electron scattering, the second electron is ionized by the $1s$ photoelectron in a $(e,2e)$ -like electron collision. The KO process, sometimes also named TS1 process, dominates at low photon energies, whereas at high photon energies the SO mechanism prevails [9,10].

Early DPI works were carried out using conventional x-ray sources [11,12]. The advent of third-generation synchrotron radiation facilities about 30 years ago providing intense, monochromatic and energy tunable x-ray beams combined with the development of modern high-energy-resolution wavelength-dispersive spectrometers (WDS) gave a new boost to the domain (see, e.g., [10,13–16]). The same holds for the more recent advent of x-ray free-electron laser (XFEL) facilities. In the XFEL case, the extremely short (a few femtoseconds), intense (about 10^{11} photons), and microfocused coherent x-ray pulses permit to produce double K -shell vacancy states via the absorption of two photons by the same atom [17–21]. In the XFEL DPI, the first and second $1s$ electrons are removed sequentially by two subsequent photons belonging to the same XFEL pulse. Actually, the pulse is so short that the second electron is removed before the first vacancy decays. Double $1s$ vacancy states can also be produced by impact with electrons. In collisions with electrons, the double K -shell ionization results mainly from shake and TS2 processes. The TS2 process corresponds to a sequential inelastic scattering of the same incoming electron on two bound electrons. Since the shake and TS2 processes are characterized by small probabilities, K hypersatellites induced by electron impact are also very weak.

Stronger K -hypersatellite signals can be obtained by bombarding the samples with heavy ions (HI). In this case, due to the strong Coulomb field of the charged projectile, several inner-shell electrons can be indeed ionized simultaneously. X-ray spectra induced by impact with heavy ions exhibit rich satellite and hypersatellite structures. As the multiple ionization cross section varies as Z_p^2 , where Z_p is the atomic number of the projectile, the satellite and hypersatellite yields resulting

from atomic collisions with heavy ions are much higher than those produced by nuclear decay processes or photon and electron impact. However, to unravel the complex structure of HI-induced x-ray spectra, the use of high-resolution detectors such as crystal spectrometers is mandatory. The first observation of $K\alpha$ hypersatellites originating from heavy-ion-atom collisions was reported by Richard *et al.* [22]. This pioneering work was followed by many other studies (see, e.g., [23–27]). Some high-resolution measurements of L and M hypersatellites of mid-heavy and heavy elements were also performed [28–30].

Energies of hypersatellite transitions are more sensitive than diagram transitions to the Breit interaction, quantum electrodynamics (QED) corrections, and relativity effects. Precise energy measurements of hypersatellite x rays are therefore very useful to probe the goodness of atomic structure calculations. From the hypersatellite-to-diagram line yield ratios, the double-to-single K -shell ionization cross-section ratios can be derived. This permits to check the reliability of the predictions from different theoretical models such as the semiclassical approximation (SCA) and classical trajectory Monte Carlo (CTMC) models. Well-established double K -shell ionization cross sections are also needed for the interpretation of the x-ray radiation from the Universe [31], for plasma diagnostics [32], for the development of new x-ray sources [33], and also for the understanding of the x-ray emission from matter irradiated by photon beams of extreme fluences such as XFEL beams [17].

The $K\alpha_1^h$ hypersatellite corresponds to the spin-flip transition $1^1S_0 \rightarrow 2^3P_1$ which is forbidden by the E1 selection rules in the pure LS coupling scheme but allowed within the jj coupling scheme. The $K\alpha_2^h$ hypersatellite corresponds to the transition $1^1S_0 \rightarrow 2^1P_1$ which is allowed by the E1 selection rules in both coupling schemes. As the LS coupling scheme applies to low- Z elements and the jj coupling to high- Z elements, the $K\alpha_1^h/K\alpha_2^h$ intensity ratio allows to probe the intermediacy of the coupling scheme across the periodic table [34,35]. Similarly, the $K\beta_1^h$ hypersatellite ($1^1S_0 \rightarrow 3^3P_1$ spin-flip transition) is forbidden by the E1 selection rules in the LS coupling scheme, whereas the $K\beta_3^h$ hypersatellite ($1^1S_0 \rightarrow 3^1P_1$ transition) is allowed so that for light elements the observed $K\beta^h$ lines correspond quasiexclusively to the $K\beta_3^h$ hypersatellites. A further interest of hypersatellite x-ray lines resides in their natural linewidths from which the mean lifetimes of double $1s$ vacancy states can be derived and compared to theory.

In this study, the $K\alpha$ hypersatellite x-ray spectra of Ca ($Z = 20$), V ($Z = 23$), Fe ($Z = 26$), and Cu ($Z = 29$) bombarded by fast C and Ne ions were measured in high-energy resolution. For Ca and V, the $K\beta^h$ hypersatellites could also be observed. The choice of the selected target elements was motivated by the fact that for these elements experimental photon- and electron-induced hypersatellite data were available, while information about HI-induced hypersatellites was still scarce in this part of the periodic table.

II. EXPERIMENT

The experiment was carried out at the Paul Scherrer Institute (PSI) in Villigen, Switzerland. The Ca, V, Fe, and Cu K -shell single- and double-vacancy states were produced by bombarding the samples with 12 MeV/amu carbon and 9 MeV/amu

neon beams. The sample x-ray emission was measured by means of high-energy-resolution x-ray spectroscopy using the von Hamos curved crystal spectrometer of Fribourg [36].

A. Spectrometer

In the von Hamos geometry, the x-ray emission from the target is diffracted by a cylindrically bent crystal and the diffracted beam is collected with a position-sensitive detector. The crystal views the target through a narrow vertical rectangular slit which is kept fixed in space and represents the effective source of radiation. The slit, front plane of the detector and axis of curvature of the crystal are all located in the same vertical plane. The dispersion axis of the spectrometer is parallel to the crystal curvature axis, whereas the cylindrical crystal curvature provides a vertical focusing of the diffracted beam, which permits to increase substantially the collection efficiency of the diffracted x rays.

For a single position of the crystal and detector, a certain angular range is subtended by the crystal so that an energy domain extending over several tens of eV can be measured with the von Hamos spectrometer in a scanless mode of operation. The covered energy domain is limited mainly by the length ℓ_{det} (in the direction of dispersion) of the employed position-sensitive detector. To cover a wider energy domain, the central Bragg angle is modified by translating the crystal and the detector along axes which are parallel to the direction of dispersion, the translation distance of the detector being twice that of the crystal.

For each crystal-detector translation, the target is also moved along an axis perpendicular to the dispersion axis so that the target remains aligned with the slit center to crystal center direction. Furthermore, the target displacement and the orientation of the slit around its vertical axis are mechanically correlated so that the slit is always perpendicular to the target-to-crystal direction. Note that the target being placed behind the slit, the target width seen by the crystal depends on the target alignment with respect to the slit-crystal direction and is significantly bigger than the slit width. This may also contribute to enhance the spectrometer luminosity in the case where the incoming particle beam is rather wide like in the present experiment. The crystal, detector, and target translations as well as the target alignment are carried out by means of remote-controlled stepping motors.

For the present experiment, the spectrometer was equipped with two crystals. For the Ca and V measurements, a LiF(200) crystal ($2d = 4.0280 \text{ \AA}$) was used while for the Fe and Cu measurements a SiO₂(2 $\bar{2}$ 3) crystal ($2d = 2.7500 \text{ \AA}$) was employed. Both crystals were 10 cm high, 5 cm wide, and 0.5 mm thick. They were glued on aluminum blocks machined to a concave cylindrical surface with a radius $R = 25.4 \text{ cm}$. For the detection of the diffracted x rays, a front illuminated deep depleted CCD camera was used. The CCD chip consisted of 1024 pixels (in the dispersion direction) \times 256 pixels (in the vertical direction) with a pixel resolution of $27 \mu\text{m}$ and a nominal depletion depth of $50 \mu\text{m}$. The CCD camera was cooled down to -60°C . Depending on the intensity of the measured x-ray lines, several hundreds to several thousands of CCD images with an exposure time of typically 1–5 s per image

TABLE I. Target thicknesses in mg/cm^2 .

Projectile	Calcium	Vanadium	Iron	Copper
C ⁴⁺	6.41	16.9	17.0	17.1
Ne ⁶⁺	1.86	2.94	3.15	2.61

were collected. During the pixels' reading, the x-ray shutter placed in front of the CCD was closed. For each sample, several energy domains (e.g., nine for Ca) corresponding to different detector positions were needed to cover the whole energy range corresponding to the K x-ray spectrum. The detector positions were chosen so that neighboring energy domains were partly overlapping.

B. Samples

The vanadium, iron, and copper targets consisted of thin 20 mm high \times 6 mm wide metallic foils with purities of 99.8+%, 99.85%, and 99.97%, respectively. For calcium, thin foils were prepared by laminating 99.0% pure lumps with an in-house roller press until the appropriate thickness was reached. The obtained samples were then cut to have the same dimensions as the metallic foils. For the measurements, each target was tilted around a vertical axis passing through the target center so that the normal to the target front surface coincided with the bisector of the angle between the incoming heavy-ion beam and the slit-to-crystal direction. This target alignment was kept at the same value for the whole K x-ray spectrum.

The intensity of the hypersatellites of interest being small as compared to those of their parent diagram lines, hypersatellite spectra with a good enough statistics required the use of rather thick samples. Too thick samples, however, would have led to large particle energy losses with two adverse side effects: first, an overheating of the targets whose temperature could reach the melting point and, second, difficulties in the interpretation of the results due to the strong variation of the heavy-ion energy in the sample. As the ionization cross section varies nonlinearly with the projectile energy, a meaningful comparison with theory requires indeed that the average projectile energy in the sample E_{av} remains reasonably close to the incident energy E_{in} . Thus, the target thicknesses were chosen (see Table I) as a compromise between a high enough intensity of the sample x-ray emission and a reasonably small loss of the projectile energy in the sample.

C. Heavy-ion beams

The C⁴⁺ and Ne⁶⁺ ions produced by a 10-GHz CAPRICE ECR source were injected into the variable energy Philips cyclotron of PSI and accelerated to final energies of 143.0 and 179.0 MeV, respectively. The intensity of the heavy-ion beams was in the range of 100–200 nA. The beam spot size on the targets was typically 9 mm high and 6 mm wide. During the deceleration of the heavy ions in the samples, most of the remaining electrons of the projectiles were removed so that the investigated collisions can be considered as collisions between neutral atoms and nearly fully stripped heavy ions.

The specific energy loss dE/ds of the projectiles in the target was parametrized by means of the following relation:

$$\frac{dE}{ds} = -cE^{-\nu}. \quad (1)$$

The constants c and ν were deduced from a double-logarithmic interpolation of the specific energy-loss values computed with the SRIM code [37]. The energy of the projectile after a penetration depth s can be deduced from Eq. (1):

$$E(s) = [E_{\text{in}}^{\nu+1} - c(\nu+1)s]^{\frac{1}{\nu+1}}, \quad (2)$$

so that the energy of the emerging projectiles is given by

$$E_{\text{out}} = E\left(s = \frac{h}{\rho \cos \phi}\right), \quad (3)$$

where h is the target thickness in g/cm^2 , ρ the target specific weight in g/cm^3 , and ϕ the angle between the normal to the target surface and the direction of the incoming heavy-ion beam.

The average projectile energy in the sample depends on the single, respectively double, K -shell ionization cross section which in turn varies as a function of the projectile energy and on the photon mass absorption coefficient of the target for the x-ray transition of interest. The average energy of the projectiles in the target was determined using the following expression:

$$E_{av} = \frac{\int_0^{\frac{h}{\cos \phi}} E\left(\frac{x}{\cos \phi}\right) \sigma_{K,KK} [E\left(\frac{x}{\cos \phi}\right)] \exp\left[-\mu(E_X) \frac{\rho x}{\sin(\vartheta+\phi)}\right] dx}{\int_0^{\frac{h}{\cos \phi}} \sigma_{K,KK} [E\left(\frac{x}{\cos \phi}\right)] \exp\left[-\mu(E_X) \frac{\rho x}{\sin(\vartheta+\phi)}\right] dx}, \quad (4)$$

where σ_K or σ_{KK} stands for the single or double K -shell ionization cross section and μ represents the mass absorption coefficient in cm^2/g for the x-ray transition of interest of energy E_X . The cross sections σ_K and σ_{KK} were calculated within the SCA model using the code IONHYD of Trautmann and Rösler [38], whereas the mass absorption coefficients were taken from the NIST database XCOM [39].

The so-obtained average energies are listed in Table II. One sees that for all collisions the average energies corresponding to the $K\alpha$ and $K\beta$ diagram lines and the $K\alpha^h$ hypersatellites are nearly the same, whereas the average energies of the $K\beta^h$ hypersatellites are slightly bigger. This is due to the fact that

the energies of the $K\beta^h$ transitions lie above the K -absorption edges, which leads to an enhanced target self-absorption for these transitions as compared to the other ones and consequently to a bigger contribution of the front parts of the targets where the projectile energy is bigger than the rear parts where the projectile energy is lower.

As shown in Table II, the energy E_{out} of the emerging projectiles varies, depending on the target species and thickness, between about 125 and 135 MeV for C and between 168 and 172 MeV for Ne. To minimize the background due to the production of nuclear reactions in the beam stopper, the latter was made of Pb. For this heavy element, the threshold energies (Coulomb barriers) for nuclear reactions lie indeed relatively high (72 and 114 MeV for the C and Ne projectiles, respectively) so that the nuclear cross sections for the above-mentioned emerging projectile energies are far below their maximum. In addition, the beam stopper was placed reasonably far from the CCD detector and a supplementary γ -ray shielding was installed between the beam stopper and the CCD detector.

III. DATA ANALYSIS

A. Energy calibration and instrumental broadening

1. Energy calibration of the spectrometer

For the energy calibration of the von Hamos spectrometer, measurements of the photoinduced $K\alpha_{1,2}$ diagram transitions of the four samples were performed. The sample fluorescence was produced using the bremsstrahlung from a Cr anode side-window x-ray tube. The reference energies of 3691.719(49) eV, 4952.916(59) eV, 6404.0062(99) eV, and 8047.8227(26) eV reported in [40] for the $K\alpha_1$ transitions of Ca, V, Fe, and Cu, respectively, were assigned to the fitted centroids of the corresponding x-ray lines. The energy calibration of the heavy-ion-induced x-ray spectra was then performed using the following formula:

$$E_i = \frac{n}{n_0} \frac{\tan(\vartheta_o)}{\tan(\vartheta_i)} \sqrt{\frac{1 + [\tan(\vartheta_i)]^2}{1 + [\tan(\vartheta_o)]^2}} E_o, \quad (5)$$

where E_i represents the energy corresponding to the pixel p_i , n and n_0 are the diffraction orders with which the x-ray spectrum to be calibrated and reference x-ray line were measured, and ϑ_o and ϑ_i stand for the Bragg angles related to the fitted centroid pixel p_0 of the reference x-ray line and pixel p_i of the heavy-ion-induced spectrum.

TABLE II. Energies of incoming and emerging projectiles for the four investigated targets as well as average projectile energies corresponding to the x-ray lines of interest. For details, see text.

Projectile	Target	Angle ϕ (deg)	E_{out} (MeV)	$E_{av}(K\alpha)$ (MeV)	$E_{av}(K\alpha^h)$ (MeV)	$E_{av}(K\beta)$ (MeV)	$E_{av}(K\beta^h)$ (MeV)
143.0 MeV C ⁴⁺	Ca	19.575	135.8	140.0	139.9	139.9	141.9
	V	27.225	125.8	136.9	136.6	136.5	141.4
	Fe	24.525	125.5	136.2	136.0	135.8	140.6
	Cu	29.250	126.0	136.1	135.9	135.8	139.9
179.0 MeV Ne ⁶⁺	Ca	19.575	172.0	175.7	175.6	175.6	176.5
	V	27.225	169.2	174.4	174.3	174.3	175.5
	Fe	24.525	168.5	174.0	174.0	173.9	174.9
	Cu	29.250	170.6	174.9	174.9	174.9	175.4

TABLE III. Experimental broadening parameter σ in eV as determined from the fits of the photoinduced $K\alpha_1$ transitions used for the energy calibration.

Projectile	Crystal	Ca $K\alpha_1$	V $K\alpha_1$	Fe $K\alpha_1$	Cu $K\alpha_1$
C ⁴⁺	LiF (200)	0.70(1)	1.15(1)		
C ⁴⁺	SiO ₂ (2̄2̄3)			0.94(2)	1.44(2)
Ne ⁶⁺	LiF (200)	0.72(1)	1.22(1)		
Ne ⁶⁺	SiO ₂ (2̄2̄3)			0.96(2)	1.34(2)

2. Instrumental broadening

For all samples, the instrumental response was found to be well reproduced by a Gaussian function. The instrumental energy broadening was determined experimentally from the fits of the above-mentioned x-ray tube-based measurements. The $K\alpha_1$ diagram x-ray transitions taken as references were fitted with Voigt functions. In the fits, the Lorentzian natural linewidths were kept fixed at the values derived from the atomic level widths recommended by Campbell and Papp [41], whereas the standard deviations σ of the Gaussians representing the instrumental response of the spectrometer were used as free-fitting parameters. The values of σ obtained from the fits are listed in Table III.

One can see in Table III that, except in one case, the instrumental broadenings σ determined during the Ne experiment are slightly bigger than those obtained during the C experiment. This is probably due to the fact that the slit was a little bit more open during the Ne measurements which were performed about one year later. As the instrumental broadening is expected to vary smoothly with the photon energy, a linear function was assumed for $\sigma(E)$.

The Gaussian width of the instrumental response is mainly due to the slit width, Darwin width of the crystal, crystal mosaicity, and spatial resolution of the detector. The slit width affects the instrumental resolution and luminosity of the spectrometer in opposite ways. In this experiment, a slit width w_{slit} of 0.2 mm was thus adopted as a compromise between a high enough energy resolution and acceptable luminosity. The energy broadening originating from the CCD is about $10\times$ smaller than the one due to the slit. For this reason, the 27- μm resolution of the CCD detector was not really needed and a software binning of four adjacent pixels' columns was performed offline in order to obtain higher count rates in the one-dimensional energy spectra.

B. Data correction and normalization

1. Beam intensity

The beam intensity was monitored by measuring the $K\alpha, \beta$ x-ray emission of the target with a 500- μm -thick Si PIN photodiode. The latter was placed on the crystal support above the crystal so that it viewed the target through the slit as the crystal. For each sample, the photodiode was oriented so that its entrance window was perpendicular to the direction defined by the slit and crystal center. Furthermore, a gate triggered by the CCD shutter signal blocked the photodiode data acquisition when the CCD shutter was closed. Thus, data were collected synchronously with the CCD detector and the photodiode. For

each target, the x-ray yields of the partial spectra corresponding to consecutive CCD positions were normalized to the intensity of the first energy region using the $K\alpha, \beta$ yields measured by the photodiode for the different regions.

2. Beam profile

In the von Hamos slit geometry, the different pixels' columns of the CCD detector do not see the same part of the sample, the pixels' columns on the left-hand side of the CCD viewing the right part of the sample and vice versa. Thus, if the intensity distribution of the heavy-ion beam on the sample is not homogeneous, the inhomogeneity is reflected in the x-ray yields measured by the CCD, which can distort the shape of the measured x-ray spectrum. However, if the beam intensity profile along the transverse direction of the sample is known, the CCD spectrum can be corrected by normalizing the intensity of each column of pixels to the intensity of a column of pixels taken as reference, using the ratio of the beam intensities integrated over the profile intervals viewed on the target by the column of pixels of interest and the column of reference.

The beam intensity profile was determined with the von Hamos spectrometer itself. A narrow vertical stripe covering the $K\alpha_1$ x-ray line was first selected on the CCD. Then, the integrated intensity of this CCD stripe was measured for several successive positions of the sample moved along the direction of the beam. Actually, moving the sample along the beam axis and measuring the intensity of the sample x-ray emission at a constant Bragg angle permits indeed to determine the horizontal distribution of the beam intensity. The so-obtained intensity points were then interpolated with a polynomial. For illustration, the beam intensity profile corresponding to the carbon-calcium collision is depicted in Fig. 1 together with the profile intervals seen by the pixels' columns 1 and 1024 for the first and ninth detector positions. The spacing between the two intervals corresponding to the first region is bigger than the one of the ninth region because the distance between the slit and the crystal center is smaller for the first region than for the ninth one.

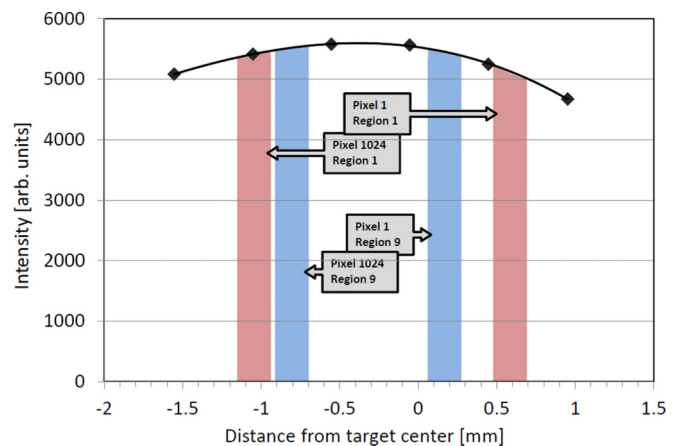


FIG. 1. C beam intensity profile employed to correct the $K\alpha$ x-ray spectrum of Ca shown in Fig. 2. The red and blue vertical stripes represent the target areas seen by the pixels' columns 1 and 1024 for the CCD positions 1 (3650–3750 eV) and 9 (4350–4450 eV).

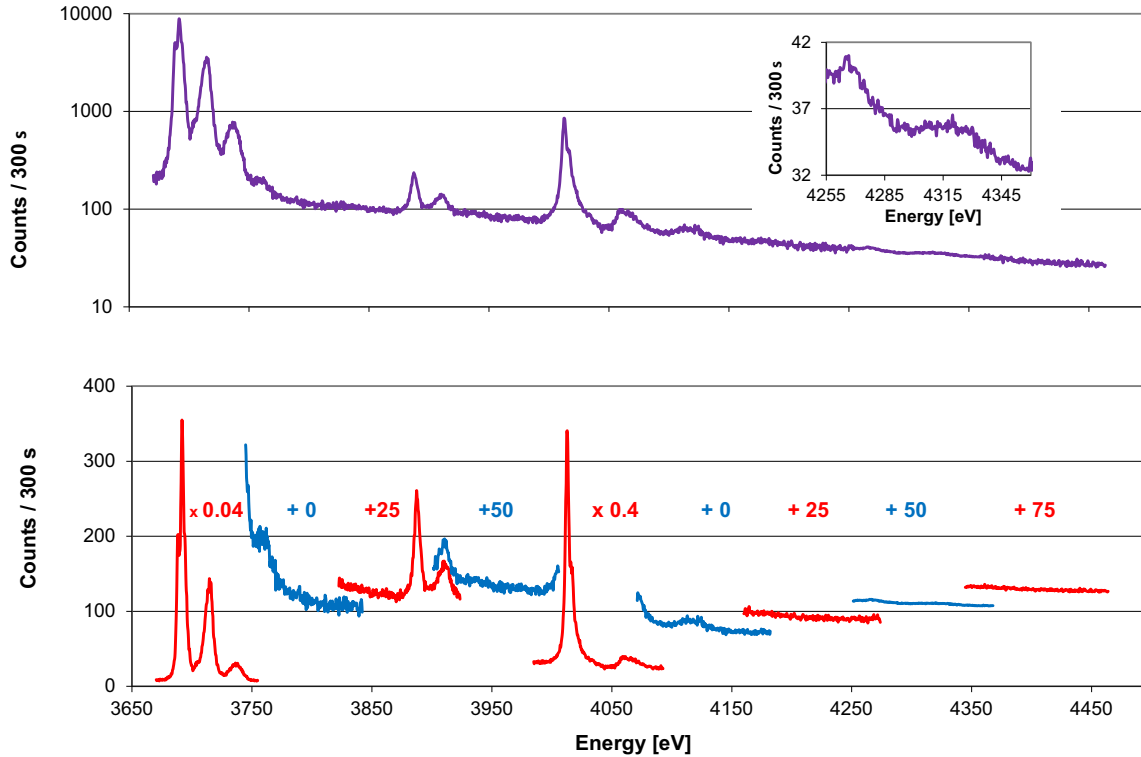


FIG. 2. Reconstructed K x-ray spectrum of Ca produced by impact with 143 MeV C ions. In the top panel, the full spectrum is represented within the same logarithmic intensity scale. For the assignments of the different peaks, see text. The energy region corresponding to the weak $K\beta^h$ spectrum is shown with an enlarged intensity scale in the inset. The partial spectra corresponding to the different CCD positions needed to cover the whole energy range are plotted in the bottom panel. In this case the intensity scale is linear but the intensities of the regions corresponding to the $K\alpha$ and $K\beta$ diagram lines were multiplied by 0.04 and 0.4, respectively, and offsets in the intensity scale were employed for the different regions to better show the overlapping regions.

3. Reconstruction of the spectra

As mentioned before, the whole energy range corresponding to the K -shell diagram, satellite, and hypersatellite lines could not be measured with a single CCD position. Therefore, the full spectra were reconstructed by putting together the partial spectra measured at several consecutive and partly overlapping CCD positions, each partial spectrum having been normalized beforehand for the differences in acquisition times and beam intensities and corrected for the beam profile according to the procedure discussed above. In some cases, some small but significant differences were observed between the intensities of overlapping energy regions. These discrepancies were explained by the small variations of the beam intensity profile that occurred between two consecutive beam profile measurements. In such cases, the $(n + 1)$ th spectrum was adjusted to the n th one by multiplying it by a scaling factor determined from the intensity ratio of the two overlapping regions.

For illustration, the reconstructed whole x-ray spectrum corresponding to the C^{4+} -Ca collision is depicted in Fig. 2 (top panel) where one can see the $K\alpha L^{-n}$ (between 3670 and 3770 eV) and $K\beta L^{-n}$ (between 3950 and 4150 eV) diagram ($n = 0$) and parent n th-order L -satellite lines. The two lines visible in the energy region between 3880 and 3970 eV correspond to the $K\alpha_2^h$ hypersatellite and $K\alpha_{1,2}^h L^{-1}$ hypersatellite L satellite, while the two weak bumps shown in

the inset correspond to the $K\beta_3^h$ hypersatellite and $K\beta_{1,3}^h L^{-1}$ hypersatellite L satellite. Note that although the $K\alpha_1^h$ and $K\beta_1^h$ hypersatellites are strictly forbidden by the E1 selection rules in the LS coupling scheme, some transitions of the $K\alpha_1^h L^{-1}$ and $K\beta_1^h L^{-1}$ hypersatellite satellites may be allowed as a result of the coupling of the angular momenta of the two K holes and the L spectator hole in the initial state and the remaining K hole with the two L holes ($K\alpha^h$), or the M hole and the L spectator hole ($K\beta^h$), in the final state. In the $K\beta$ hypersatellite region (4255–4355 eV), the statistical fluctuations are smaller because this region was measured with a significantly longer acquisition time. The bottom panel of Fig. 2 shows the partial spectra corresponding to the nine different CCD positions needed to cover the full energy range of interest.

C. Fitting procedure

The spectra were analyzed by means of a least-squares-fit method using the software package PEAKFIT®. As the natural line shape of an x-ray transition corresponds to a Lorentzian function and the instrumental broadening can be well reproduced by a Gaussian, Voigt profiles which result from the convolution of Gauss and Lorentz functions [42] were employed to reproduce the shapes of the measured x-ray lines.

For each spectrum, the energies, Lorentzian widths, and intensities of the measured lines as well as the parameters of

the linear background were used as free-fitting parameters, whereas the standard deviation of the instrumental response was kept fixed at the value determined by interpolation from the known linear function $\sigma(E)$ (see Sec. III A 2). However, due to the number of transitions to be analyzed in each spectrum and the intensities of the transitions of interest which covered several orders of magnitude, convergence problems were encountered during the fitting procedure. In order to circumvent these difficulties, the following steps were taken.

The reconstructed spectra were divided into several parts containing structures of comparable intensities. The energies and Lorentzian widths of the most intense x-ray lines were first extracted by fitting the first part of the spectrum and the obtained values were then used as fixed parameters in the fit of the other parts. Finally, the whole spectrum was fitted simultaneously while releasing progressively the previously fixed parameters. Such an iterative procedure allowed us to obtain in most cases a steady convergence of the fits.

The goodness of the fits was probed by comparing the intensity ratios $I(K\alpha_2)/I(K\alpha_1)$ obtained from the fits to the values quoted in the tables of Scofield [43]. The same was done for the $I(K\beta_{1,3})/I(K\alpha_{1,2})$ yield ratios. In this case, however, the intensities of the $K\beta_{1,3}$ transitions were corrected beforehand for the change of the target self-absorption, crystal peak reflectivity, and CCD efficiency (see Sec. III D). The natural widths of the diagram $K\alpha_1$ and $K\alpha_2$ lines were also kept fixed in these fits at the values recommended by Campbell and Papp [41]. This was necessary to get correct $K\alpha_{1,2}$ intensities because the close-lying M -satellite structures could not be resolved, the energy shifts of these satellites being smaller than the natural linewidths of the parent diagram lines. The L -satellite structures were fitted using a number of components as small as possible in order to shorten the fitting time. This was a reasonable choice since the L -satellite transitions did not represent the main interest of this study.

To get reliable results for the intensities of the weak hypersatellites, a particular attention was devoted to the background in the fits of the hypersatellite spectra. The high-energy tails of the intense $K\alpha_{1,2}$ diagram and $K\alpha_{1,2}L^{-n}$ satellite lines which occur below the $K\alpha^h$ hypersatellites as well as the low-energy tails of the $K\beta_{1,3}$ diagram and $K\beta_{1,3}L^{-n}$ satellite lines which occur above were included in the fits, keeping their energies, widths, and intensities at the values provided by the fits of the corresponding regions.

M satellites which are not resolved from their parent diagram lines but appear as slight asymmetries on the high-energy sides of the latter were considered in the fits of the diagram lines with additional Voigtians. The energy separation between the $(n + 1)$ -th- and n -th-order M satellites was assumed to be nearly constant for any value of n and equal to the energy difference between the first-order M satellite and the parent diagram line. The latter energy difference was deduced from the corresponding photoinduced spectrum where first-order M satellites were also observed as a result of shake processes. The intensity of the first-order M satellite was let free in the fit while the relative intensities of the higher-order satellites were kept fixed at values determined from the intensity of the first satellite assuming a binomial distribution for the M -satellite yields.

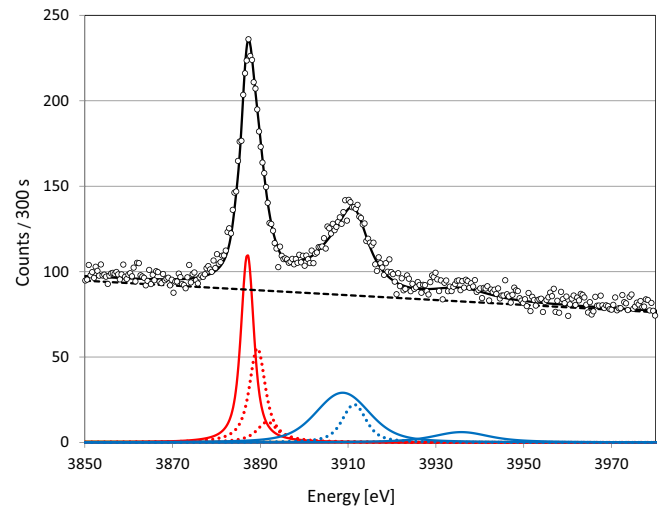


FIG. 3. Fit of the C-induced $K\alpha$ hypersatellite spectrum of Ca. The top part of the figure shows the measured spectrum (open circles), the linear background (dashed black line), and the total fit (black curve). The fitted components are depicted in the lower part where the red solid line represents the $K\alpha_2^h$ hypersatellite, the blue solid lines the first- and second-order L satellites of the $K\alpha_{1,2}^h$ hypersatellites, and the red and blue dotted lines the M satellites accompanying the above-mentioned transitions. The fitted $K\alpha_1^h$ hypersatellite is too weak to be seen.

As $K\alpha_1^h$ hypersatellites are hindered by the electric-dipole (E1) selection rules in the LS coupling scheme and because this scheme prevails for light elements, $K\alpha_1^h$ hypersatellites are significantly weaker than $K\alpha_2^h$ hypersatellites for low- Z elements as those investigated in the present experiment. For this reason, the $K\alpha_1^h$ lines were difficult to extract from the background and the partly overlapping $K\alpha_{1,2}^h L^{-1}$ satellite structure. Good initial guess values which were taken from available literature references were thus needed for the energies and relative intensities of these weak transitions. The guess values were first kept fixed in the fitting procedure and, whenever possible, let free in subsequent iterations. Note that, as mentioned in Sec. I, in the LS coupling only the $K\alpha_1^h L^0 M^0$ transitions are strictly forbidden by the E1 selection rules. Additional vacancies, especially in the L shell, can significantly relax these rules.

As examples, the fits of the C- and Ne-induced $K\alpha^h$ x-ray spectra of Ca are presented in Figs. 3 and 4, respectively. In the C-induced spectrum, the well-defined $K\alpha_2^h$ hypersatellite line (at 3885 eV) was fitted with one Voigtian whose energy, intensity, and Lorentzian width were used as free-fitting parameters. The M -satellite structure of the latter transition could be well reproduced with two Voigtians (dotted lines). The second bump around 3910 eV was fitted with two Voigtians, one for the $K\alpha_{1,2}^h L^{-1} M^0$ transitions and another one for the $K\alpha_{1,2}^h L^{-1} M^{-n}$ transitions, whereas the third bump at 3940 eV corresponding to the $K\alpha_{1,2}^h L^{-2} M^{-n}$ transitions and the extremely weak $K\alpha_1^h$ hypersatellite (at about 3892 eV) could be fitted each with a single Voigtian. In the case of the $K\alpha_1^h$ hypersatellite, however, due to the very small intensity of this line, only the energy could be let free. The Lorentzian

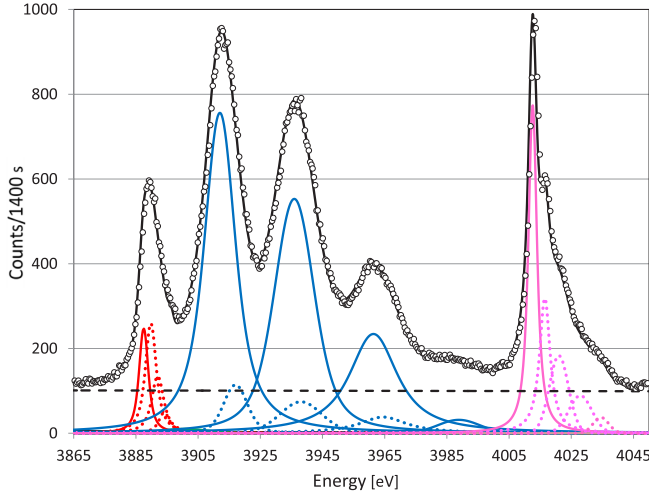


FIG. 4. Same as Fig. 3 but for the Ne-induced spectrum. The pink solid line (around 4015 eV) corresponds to the $K\beta$ diagram line and the pink dotted lines to the $K\beta M^{-n}$ ($n = 1, \dots, 4$) satellites.

width was kept fixed at the same value as the one of the $K\alpha_2^h$ hypersatellite using the *share* option provided by the PEAKFIT® program, and its intensity was fixed to 2.3% of that of the $K\alpha_2^h$ transition according to the theoretical intensity ratio reported in Ref. [44].

As the multiple ionization cross section increases with the squared atomic number of the projectile, the K hypersatellites and their L - and M -satellite structures observed in the Ne-induced spectrum are much stronger than in the corresponding C-induced spectrum. As shown in Fig. 4, the $K\alpha_2^h$ hypersatellite was fitted with four components, one for the hypersatellite and three for the unresolved M -satellite structure. The $K\alpha_{1,2}^h L^{-n}$ ($n = 1, \dots, 3$) satellites could be well reproduced with two Voigtians per peak, whereas for the $K\alpha_{1,2}^h L^{-4}$, a single Voigtian was needed. As the first-order L satellite of the $K\alpha_{1,2}^h$ hypersatellite is much stronger than the underlying $K\alpha_1^h$, any attempt to fit the weak hypersatellite was found to be hopeless so that the energy, natural width, and relative intensity of this line had to be kept fixed in the final fit of the hypersatellite spectrum.

D. Intensity correction factors

In order to get correct hypersatellite-to-diagram line yield ratios, the solid angle of the spectrometer and the effective size of the source which vary as a function of the photon energy must be considered. The same holds for the crystal-peak reflectivity, the efficiency of the CCD detector, and the absorption in the target of the x rays of interest.

1. Solid angle of the spectrometer and effective source size

In the von Hamos geometry, the solid angle of the spectrometer varies with the Bragg angle and the one-dimensional energy spectra corresponding to the sums of the filtered two-dimensional CCD images projected onto the dispersion axis have to be corrected to account for this variation. For a given

Bragg angle, i.e., photon energy, the solid angle reads as

$$\Omega(E) = \int_{-\Delta\vartheta_D(E)/2}^{\Delta\vartheta_D(E)/2} \int_{\alpha_{\min}(E)}^{\alpha_{\max}(E)} \sin(\theta) d\theta d\psi. \quad (6)$$

In the above formula, $\alpha_{\min}(E) = [\pi - \alpha_{av}(E)]/2$, $\alpha_{\max}(E) = [\pi + \alpha_{av}(E)]/2$, and $\Delta\vartheta_D(E)$ represents the Darwin width for the photon energy E . The angle $\alpha_{av}(E)$ is defined by

$$\alpha_{av}(E) = 2 \arctan \left[\frac{h_{av}(E)}{2\ell(E)} \right], \quad (7)$$

where $h_{av}(E)$ represents the average height of the crystal seen by the active part of the target contributing to the production of the observed fluorescence and the length $\ell(E)$ is defined by

$$\ell(E) = \frac{R}{\sin[\vartheta(E)]} + \frac{d}{\cos[\vartheta(E)]}, \quad (8)$$

where R is the radius of curvature of the crystal, d the distance from the slit to the sample translation axis, and ϑ the Bragg angle. The Darwin widths were calculated with the computer code XOP (x-ray oriented programs) [45]. In the calculation of the solid angle, the height h of the crystal was replaced by $h_{av}(E)$ because, depending on the detector position, some points of the target may not see the full height of the crystal but only a part of it. To calculate $h_{av}(E)$, the vertical coordinates of the target points seen by the top and bottom pixels of the considered CCD column were calculated. The obtained target height $h_t(E)$ was compared to the height of the beam spot h_{beam} and the effective height of the radiation source $h_{\text{eff}}(E)$ was determined by the condition $h_{\text{eff}}(E) = \text{Min}[h_t(E), h_{\text{beam}}]$. The effective source height $h_{\text{eff}}(E)$ was then divided into 1000 small vertical segments and the crystal height seen by each segment considered as a pointlike source was computed. Finally, $h_{av}(E)$ was determined by calculating the average value of the 1000 partial heights.

As mentioned above, the effective height of the radiation source varies as a function of the photon energy, i.e., the Bragg angle ϑ . The same holds for the source width $w_{\text{eff}}(E)$. The latter is given by

$$w_{\text{eff}}(E) = \frac{w_{\text{slit}}}{\sin[\vartheta(E) + \phi]}. \quad (9)$$

The effective area of the photon source is then

$$S_{\text{eff}}(E) = h_{\text{eff}}(E)w_{\text{eff}}(E). \quad (10)$$

The solid angles Ω and effective source areas S_{eff} computed for the x-ray lines of interest are presented in Table IV.

2. Crystal-peak reflectivity

The peak reflectivities R_p of the two crystals were calculated for each transition of interest with the XOP software package [45]. As K x rays are not polarized, the average values of the peak reflectivities provided by the XOP code for photons linearly polarized in the horizontal plane (s -polarized x rays) and vertical plane (p -polarized x rays) were used. The obtained values are listed in Table IV. Note that for p -polarized x rays, the peak reflectivity tends to zero when the Bragg angle approaches 45° . This explains the abrupt decrease of the peak reflectivity of the LiF crystal for the $K\beta^h$ hypersatellite of Ca ($\vartheta = 46.2^\circ$) and the small peak reflectivities of the SiO_2 crystal

TABLE IV. Solid angles Ω in μsr , effective source areas S_{eff} in mm^2 , crystal-peak reflectivities R_P , CCD efficiencies ϵ_{CCD} , and target activity ratios A/A_0 for the x-ray transitions of interest. The total correction factors F_{tot} with respect to the $K\alpha$ diagram lines are also quoted. For details, see text.

Crystal	Target	x-ray line	Ω	S_{eff}	R_P	ϵ_{CCD}	A/A_0^{a}	A/A_0^{b}	$F_{\text{tot}}^{\text{a}}$	$F_{\text{tot}}^{\text{b}}$
LiF(200)	Ca	$K\alpha$	12.11	1.85	0.923	0.902	0.631	0.868	1.000	1.000
		$K\alpha^h$	10.15	1.89	0.892	0.909	0.661	0.881	1.145	1.181
		$K\beta$	9.27	1.92	0.859	0.912	0.680	0.889	1.241	1.306
		$K\beta^h$	9.53	1.97	0.656	0.917	0.156	0.459	6.680	3.123
LiF(200)	V	$K\alpha$	5.85	1.98	0.920	0.920	0.467	0.861	1.000	1.000
		$K\alpha^h$	5.55	2.01	0.944	0.917	0.495	0.874	0.958	1.000
		$K\beta$	5.25	2.04	0.957	0.912	0.532	0.886	0.921	1.019
		$K\beta^h$	5.49	2.08	0.969	0.903	0.093	0.465	4.927	1.817
SiO ₂ (223)	Fe	$K\alpha$	1.77	1.92	0.432	0.782	0.563	0.890	1.000	1.000
		$K\alpha^h$	1.49	1.95	0.501	0.760	0.587	0.899	0.995	1.027
SiO ₂ (223)	Cu	$K\alpha$	0.872	2.01	0.779	0.643	0.636	0.928	1.000	1.000
		$K\alpha^h$	0.778	2.04	0.821	0.619	0.658	0.934	1.052	1.081

^aC⁴⁺ ions.

^bNe⁶⁺ ions.

for the Fe $K\alpha^h$ hypersatellite ($\vartheta = 42.6^\circ$) and especially the Fe $K\alpha$ diagram line ($\vartheta = 44.8^\circ$). In the latter case, the peak reflectivity for p -polarized x rays is indeed negligibly small (0.08%).

3. CCD efficiency

For tender x rays ranging between 3.5 and 8.5 keV which lie far above the K -absorption edge of Si, the CCD efficiency is expected to vary only smoothly with the photon energy. The CCD efficiency ϵ_{CCD} was determined using the following formula:

$$\epsilon_{\text{CCD}} = \exp \left[-\mu_{\text{SiO}_2}(E_X) \rho_{\text{SiO}_2} \frac{h_{\text{SiO}_2}}{\sin(\vartheta)} \right] \times \left\{ 1 - \exp \left[-\mu_{\text{Si}}(E_X) \rho_{\text{Si}} \frac{h_{\text{Si}}}{\sin(\vartheta)} \right] \right\}, \quad (11)$$

where $\mu_{\text{SiO}_2}(E_X)$ and $\mu_{\text{Si}}(E_X)$ represent the total mass attenuation coefficients of SiO₂ and Si for the x-ray energy E_X , ρ_{SiO_2} , and ρ_{Si} the specific weights of SiO₂ and Si, h_{SiO_2} and h_{Si} the thicknesses of the thin silicon dioxide layer and silicon chip, and ϑ the Bragg angle. The first term of the equation reflects the absorption of the x rays by the thin SiO₂ layer which is always present on the surface of front-illuminated CCD chips. The front-illuminated deep depleted CCD camera employed in the present experiment was already fully characterized in a previous project [46]. In this former work, thicknesses $h_{\text{SiO}_2} = 1 \mu\text{m}$ and $h_{\text{Si}} = 40 \mu\text{m}$ were found. The latter values were thus used in Eq. (11), while the mass attenuation coefficients were taken from the XCOM database [39]. The CCD efficiencies obtained from Eq. (11) are listed in Table IV.

4. Target self-absorption

For target thicknesses of a few mg/cm^2 as the ones used in the present experiment, the absorption of the sample x rays by the target itself is not negligible. This so-called self-absorption effect varies with the energy of the emitted x rays and has thus to be also taken into account to get reliable hypersatellite-to-

diagram line intensity ratios. The correction is, however, not straightforward because the target activity is not constant along the depth axis. The ionization cross section depends indeed on the projectile energy and the latter decreases with the target depth.

The ratio of the real target activity A to the activity A_0 of an ideal target with no absorption was determined with the following equation:

$$\frac{A}{A_0} = \frac{\int_0^{h/\rho} \sigma_{K,KK} \left[E \left(\frac{x}{\cos\phi} \right) \right] \exp \left[-\mu(E_X) \rho \frac{x}{\sin(\vartheta+\phi)} \right] dx}{\int_0^{h/\rho} \sigma_{K,KK} \left[E \left(\frac{x}{\cos\phi} \right) \right] dx}, \quad (12)$$

where σ_K and σ_{KK} represent the single and double K -shell ionization cross sections, μ the mass absorption coefficient in cm^2/g for the x-ray line of energy E_X , ρ the specific weight of the target in g/cm^3 , and ϑ and ϕ the Bragg angle and target alignment angle, respectively. The mass absorption coefficients were taken from the NIST database XCOM [39] and the cross sections σ_K and σ_{KK} were calculated within the SCA model using the code IONHYD of Trautmann and Rösel [38]. The energy $E(s)$ of the projectiles at the target depth s was calculated using the formula (2) presented in Sec. IIC. The ratios A/A_0 derived from Eq. (12) are presented in Table IV. As shown, for Ca and V the self-absorption effects are the biggest for the $K\beta^h$ hypersatellite lines because these transitions lie above the corresponding K -absorption edges where an abrupt and big increase of the mass attenuation coefficient μ occurs. Furthermore, the corrections are more pronounced for the collisions with the C ions than with the Ne ions because about five times thinner samples were used in the Ne measurements (see Table I).

The total correction factors F_{tot} listed in the two last columns of Table IV for the two projectile species indicate the numbers by which the fitted x-ray line intensities should be multiplied to account for the above-mentioned corrections. The F_{tot} values were normalized to give 1 for the $K\alpha$ diagram lines.

TABLE V. Energy shifts $\Delta\alpha_2$, $\Delta\alpha_1$, and $\Delta\beta_{1,3}$ obtained in this work. Experimental and theoretical values from other sources as well as the shifts derived from the approximation (13) are also quoted for comparison. All values are in eV.

Target		Present	Other expt.	Theory	Eq. (13)
Ca	$\Delta\alpha_2$	199.6(4)	199.4(1) [10]	197.8 [47]	205
	$\Delta\alpha_1$	207.1(1.9)	208.1(2) [10]	205.8 [47]	206
	$\Delta\beta_{1,3}$	256.5(9)		254.2 [48]	256
V	$\Delta\alpha_2$	233.4(1)	233.0(1) [10]	231.6 [47]	235
	$\Delta\alpha_1$	241.3(3)	239.8(1) [10]	238.6 [47]	237
	$\Delta\beta_{1,3}$	296.5(9)		295.4 [48]	294
Fe	$\Delta\alpha_2$	267.1(1)	268.7(1) [16]	266.3 [47]	267
	$\Delta\alpha_1$	272.6(9)	274.8(2) [16]	272.0 [47]	269
Cu	$\Delta\alpha_2$	302.7(7)	301.3(1) [16]	301.9 [47]	295
	$\Delta\alpha_1$	307.1(8)	304.8(2) [16]	305.6 [47]	299

IV. RESULTS AND DISCUSSION

A. Hypersatellite energy shifts

Although absolute energies are useful for x-ray spectroscopy, energy shifts are more adequate for comparison with theory because they permit to cope with the difficulties related to the origin of the energy scale. The energy shifts $\Delta\alpha_1$, $\Delta\alpha_2$, and $\Delta\beta_{1,3}$ of the $K\alpha_1^h$, $K\alpha_2^h$, and $K\beta_{1,3}^h$ hypersatellites with respect to their parent diagram lines obtained in this work are presented in Table V where they are compared to the experimental values determined with synchrotron radiation by Hoszowska *et al.* [10] for Ca and V and Diamant *et al.* [16] for Fe and Cu. Theoretical energy shifts from Costa *et al.* are also listed for the $K\alpha_{1,2}^h$ [47] and $K\beta_{1,3}^h$ [48] hypersatellites. The mean deviation (absolute value) between our shifts and the experimental ones from [10,16] is 1.4 eV, whereas the average value of the combined errors is about two times smaller (0.6 eV). This indicates that the uncertainties of our results, or the ones quoted in [10,16], might be somewhat underestimated. On the other hand, the shifts predicted by the multiconfiguration Dirac-Fock (MCDF) calculations of Costa [47,48] are systematically smaller than present experimental values (in average -1.8 eV for Ca, -1.9 eV for V, -0.7 eV for Fe, and -0.8 eV for Cu). It seems, however, that the theoretical predictions are improved when the open-shell valence configuration (OVC) and outer-shell ionization and excitation (OIE) effects discussed in [49] are included in the MCDF calculations. For instance, for Ca the energy shift $\Delta\alpha_2$ we have obtained using such upgraded MCDF calculations is 199.3 eV, a value in good agreement with our result and the one reported in [10].

The energy shifts of the $K\alpha$ hypersatellites were also estimated using the following approximation:

$$\Delta\alpha(Z) = \epsilon_K [E_{1s^{-1}}(Z+1) - E_{1s^{-1}}(Z)] - \epsilon_L [E_{2p^{-1}}(Z+1) - E_{2p^{-1}}(Z)], \quad (13)$$

where $E_{1s^{-1}}$ and $E_{2p^{-1}}$ represent the absolute values of the binding energies of the $1s$ and $2p$ electrons, while ϵ_K and ϵ_L are real numbers comprised between 0 and 1 which account for the diminution of the screening felt by the $1s$ and $2p$ electrons, respectively, as a result of the removal of the second

K -shell electron. For $3d$ transition elements, the constant ϵ_K was found to be 0.570 [16]. The coefficient ϵ_L which is not known was determined from our experimental shifts $\Delta\alpha_2$ by means of a least-squares-fit method. A result of 0.995 ± 0.055 was found so that a value of 1 was adopted. The same method was employed for the calculation of the energy shifts of the $K\beta^h$ hypersatellites. The single change consisted in replacing ϵ_L by ϵ_M and E_{2p} by E_{3p} in Eq. (13). A value of 1 was again assumed for ϵ_M . Using Eq. (13) and the electron binding energies reported in [50] one gets the energy shifts presented in the last column of Table V. As it can be seen, the results look reasonable in view of the crude approximations employed, the observed relative deviations being in the order of 1%.

B. Hypersatellite linewidths

The Lorentzian widths of the weak $K\alpha_1^h$ hypersatellites had to be kept fixed in the data analysis to get reliable fits. The $K\alpha_1^h$ widths were fixed at the same values as the ones of the stronger $K\alpha_2^h$ hypersatellites. This is justified because the differences between the widths of the L_2 and L_3 atomic levels are small [41] with respect to the total widths of the hypersatellites. On the other hand, for $3d$ transition elements, it is well known that the $K\beta_{1,3}$ x-ray lines evince strong asymmetries on their low-energy sides. Such asymmetries being due to nonlifetime effects, the full widths at half maximum of these transitions can no longer be interpreted as natural linewidths. Similar asymmetries are also expected for the $K\beta_{1,3}^h$ hypersatellites even if the asymmetries in this case are somewhat smeared out by the bigger linewidths of the hypersatellites as compared to those of the parent diagram lines. For these reasons, only the natural linewidths of the $K\alpha_2^h$ hypersatellites are discussed hereafter.

Remembering that the linewidth of an x-ray transition is given by the sum of the natural widths of the initial and final atomic levels and assuming furthermore that the mean lifetime of a double K -shell vacancy state is two times shorter than the one of the singly ionized K -shell state [51], i.e., that $\Gamma_{KK} \cong 2\Gamma_K$, the width of the $K\alpha_2^h$ hypersatellite transition reads as

$$\Gamma(K\alpha_2^h) \cong 3\Gamma_K + \Gamma_{L_2}, \quad (14)$$

where Γ_K and Γ_{L_2} stand for the widths of the K and L_2 atomic levels.

The Lorentzian widths of the $K\alpha_2^h$ hypersatellites obtained in this work are presented in Table VI together with other existing experimental and theoretical values. Present widths correspond to the average values of the Lorentzian widths

TABLE VI. Natural linewidths in eV of the $K\alpha_2^h$ hypersatellites obtained in this work by averaging the Lorentzian widths provided by the fits for the two beams. Other available experimental (Expt.) and theoretical (Theory) values are also quoted for comparison as well as the widths derived from Eq. (14).

Target	Present	Expt. [10]	Expt. [16]	Theory [49]	Eq. (14)
Ca	4.4(2)	3.72(18)		3.63	2.52
V	5.9(2)	5.54(19)	5.5(1)	5.46	3.66
Fe	7.3(4)		6.1(2)	6.46 ^a	4.71
Cu	7.4(8)		6.9(8)	7.09 ^b	5.51

^aLinear interpolation between Cr ($Z = 24$) and Co ($Z = 27$).

^bLinear interpolation between Co ($Z = 27$) and Zn ($Z = 30$).

obtained with the C and Ne beams. In general, the differences between the widths obtained with the two beams were found to be nearly equal to the combined errors, i.e., to the errors quoted in brackets in the second column of Table VI. The experimental values reported in the third and fourth columns were determined using synchrotron radiation. One can note that for V, the single common element investigated in [10,16], the two results are fully consistent and nearly consistent with ours but in general our widths are systematically bigger than those obtained with synchrotron radiation. This is due to the fact that the Voigtians used to fit the partly unresolved *M*-satellite structures of the hypersatellites did not reproduce the real shapes of the satellites very accurately and the widths of the Lorentzians employed to fit the hypersatellites were probably slightly enlarged by the overlapping *M*-satellite components. The theoretical predictions listed in the fifth column were taken from [49]. In these calculations whose results are in general in satisfactory agreement with the experimental values from [10,16] but again somewhat smaller than present results, the influences of the OVC and OIE effects were taken into consideration. Predictions based on the approximation (14), in which the values recommended by Campbell and Papp [41] for the widths of the *K* and *L*₂ levels were employed, are quoted in the last column. As shown, they are clearly too small but this is not surprising, as all measurements of x-ray (see [10] and references therein) and Auger [52] hypersatellite widths performed so far have led to the conclusion that the approximation (14) underestimates significantly the real linewidths of hypersatellites.

C. Hypersatellite relative intensities

The *Kα* hypersatellite-to-parent diagram line intensity ratios deduced from the fits are presented in the second and third columns of Table VII. As mentioned before, the intensities of the unresolved *M* satellites and the ones of the parent diagram or hypersatellite lines could not be unambiguously assigned in the fitting procedure. This resulted in somewhat too big Lorentzian widths of the heavy-ion-induced diagram and hypersatellite lines. For this reason, the quoted yield ratios were determined by considering the sums of the diagram or hypersatellite line intensities and those of the corresponding unresolved *M* satellites. The uncertainties quoted in the brackets of the second and third columns correspond to the

TABLE VII. Relative intensities of the *Kα* hypersatellites in percent. Errors on the last digits are given in parentheses. Values presented in columns 2 and 3 were obtained from the fitted intensities, those given in columns 4 and 5 correspond to the latter ratios corrected to account for the spectrometer solid angle, effective source size, target self-absorption, crystal reflectivity, and CCD efficiency.

Target	$I(K\alpha_{1,2}^h)/I(K\alpha_{1,2})$		$[I(K\alpha_{1,2}^h)/I(K\alpha_{1,2})]_{cor}$	
	C ⁴⁺	Ne ⁶⁺	C ⁴⁺	Ne ⁶⁺
Ca	2.38(25)	6.33(74)	2.72(46)	7.48(1.21)
V	1.97(20)	4.78(79)	1.89(33)	4.78(95)
Fe	1.66(21)	4.15(43)	1.65(31)	4.26(65)
Cu	1.35(16)	3.46(49)	1.42(25)	3.74(68)

combined errors from the fits and to the uncertainties related to the correction factors (beam intensity and beam profile) applied to the measured spectra before the fitting procedure (see Sec. III B), correction factors for which a total relative uncertainty of 10% was assumed.

The additional corrections accounting for the solid angle of the spectrometer, effective size source, crystal reflectivity, CCD efficiency, and target self-absorption were applied after the fitting procedure using the correction factors F_{tot} quoted in Table IV. The so-obtained corrected intensity ratios are listed in the right part of Table VII. Here, uncertainties of 5% were assumed for the solid angle, effective source size, and CCD efficiency corrections while an uncertainty of 10% was guessed for the crystal-peak reflectivity corrections. For the self-absorption correction, an accuracy of 10% was estimated for the XCOM mass attenuation coefficients [39], which resulted in relative uncertainties varying from 1.0% (Ne-Cu collision) up to 9.1% (C-V collision) for the self-absorption correction factors.

Relative uncertainties close to 100% or even bigger were found for the corrected $K\beta_{1,3}^h/K\beta_{1,3}$ yield ratios of Ca and V. This is due to the fact that the errors on the fitted $K\beta_{1,3}^h$ intensities, which are already large due to the poor intensities of these transitions, become still bigger when multiplied by the corresponding self-absorption correction factors. As the $K\beta_{1,3}^h$ hypersatellites lie above the *K*-absorption edges, the corresponding correction factors are indeed huge, in particular for the measurements performed with the C beam for which thicker targets were employed. For this reason, the *Kβ* hypersatellite-to-parent diagram line yield ratios were not included in Table VII, the obtained values being not reliable enough for a relevant comparison with the corresponding $K\alpha^h/K\alpha$ yield ratios.

For the collisions for which the $K\alpha_1^h$ intensity could be left free in the fitting procedure, the $K\alpha_1^h$ to $K\alpha_2^h$ yield ratios were also determined. The results are presented in Table VIII together with other existing experimental and theoretical values. As shown, a nice agreement is observed in most cases.

D. Double-to-single ionization cross-section ratios

The ratio of the double-to-single *K*-shell ionization cross sections can be written as

$$\frac{\sigma_{KK}}{\sigma_K} = \left[\frac{I(K\alpha^h)}{I(K\alpha)} \right]_{cor} \times \frac{\omega_K}{\omega_{KK}}. \tag{15}$$

TABLE VIII. Ratios in percent of the $K\alpha_1^h$ to $K\alpha_2^h$ hypersatellite intensities obtained in this work. For comparison, experimental values reported in [10,16] and theoretical predictions from [47,53] are also quoted.

Target	Present		Other expt.		Other theory	
	C	Ne	[10]	[16]	[47]	[53]
Ca	2.8(9)		3.5(1.3)		2.7	2.9
V	7.1(1.2)		7.7(1.5)	8(1)	9.9	11.8 ^a
Fe	14.5(2.4)	12.6(1.4)			16(3)	18.9
Cu	31.3(1.8)	32.6(9.1)			29(2)	32.5
					32.5	34.9 ^b

^aLinear interpolation between Ti (*Z* = 22) and Cr (*Z* = 24).

^bLinear interpolation between Fe (*Z* = 26) and Zn (*Z* = 30).

Inserting in Eq. (15) the corrected intensity ratios $[I(K\alpha^h)/I(K\alpha)]_{\text{cor}}$ listed in Table VII and the ratios ω_K/ω_{KK} (see Table X) determined from the singly and doubly ionized K -shell fluorescence yields reported in Refs. [54] and [53], respectively, the double-to-single K -shell ionization cross-section ratios could be determined. The results are presented in Table X (collisions with C ions) and Table XI (collisions with Ne ions). For comparison, the corresponding ratios obtained from calculations performed with the semiclassical approximation (SCA) and from classical trajectory Monte Carlo (CTMC) simulations are also quoted.

In the investigation of the K -shell ionization induced by impact with charged particles, it is usual to introduce the so-called reduced velocity η_K of the projectile which is defined by

$$\eta_K = \frac{v_p^2}{u_K^2} \cong 40.4 \frac{E_p^*}{(Z - S_K)^2}, \quad (16)$$

where v_p is the projectile velocity and u_K the orbital velocity of the K -shell electron in the target atom, E_p^* the specific kinetic energy of the projectile in MeV/amu, Z the atomic number of the target atom, and S_K the Slater screening factor for the K shell ($S_K = 0.3$).

The rapidity ξ_K of the collision is defined as the ratio of the time needed by the projectile to traverse the K shell of the target atom (r_K/v_p) and the characteristic time of the K -shell electron (\hbar/E_K) [55]. Thus, the parameter ξ_K reads as

$$\xi_K = \frac{r_K}{\frac{v_p}{E_K}} = \frac{2}{\theta_K} \sqrt{\eta_K}, \quad (17)$$

where r_K is the radius of the K shell, E_K the binding energy (absolute value) of the K -shell electron, and θ_K the so-called external screening factor for the target K -shell electron [55].

The collision is said slow when $\xi_K \ll 1$ and fast when $\xi_K \gg 1$. When the rapidity parameter $\xi_K \cong 1$, the collisions are referred to as intermediate velocity collisions. The values η_K and ξ_K of the collisions studied in this work are presented in Table IX. As shown, for all collisions the rapidity parameter is bigger than 1 but not much bigger. As a consequence, the investigated collisions can be considered as moderately fast. For such collisions, the inner-shell ionization is dominated by two processes, namely, the direct Coulomb ionization (DCI), denominated also impact-induced ionization, and the electron capture (EC). The probability to remove the second $1s$ electron by a shake or TS1 process is indeed negligibly small as compared to the probabilities of the DCI and EC processes. For example, in the case of the Ne-Ca collision, the double-to-

single ionization cross-section ratio σ_{KK}/σ_K corresponding to the sum of the shake and TS1 processes was estimated using the photoionization data reported in [10] to be about 9×10^{-4} , i.e., more than 80 times smaller than the experimental ratio σ_{KK}/σ_K obtained in this work (see Table XI).

In the DCI process, the ionization is due to the Coulomb interaction between the charged projectile and the bound electrons of the target atom. Several bound electrons can be involved simultaneously in the interaction so that the target atom is usually left in a multiply ionized state after the collision. In the EC process, one or more bound electrons of the target atom can be captured by the bare or nearly bare projectile. Actually, as the electron capture probability varies as n_p^{-3} [56], where n_p is the principal quantum number of the projectile level into which the electron is captured, the EC into the $1s$ orbital of the projectile prevails and the EC process contribution is only sizable in the case of fully stripped ions or H-like ions.

In our experiment, the initial charges of the C and Ne ions were 4+ and 6+, respectively. However, when energetic ions travel through a medium, their charge state varies as a function of the penetration depth and, after a very short penetration depth (a few tens of $\mu\text{g}/\text{cm}^2$), a charge equilibrium which is independent from the initial charge state of the ion is attained. The average charge equilibrium Z_{av} of an ion traveling through a medium can be approximated using the following empirical relation [57,58]:

$$Z_{av} = Z_p \left[1 + \left(\frac{3.86 \sqrt{E_{\text{out}}/M_p}}{Z_p^{0.45}} \right)^{-1/0.6} \right]^{-0.6}, \quad (18)$$

where Z_p and M_p are the atomic number and atomic mass number of the projectile and E_{out} the kinetic energy (in MeV) of the latter at the exit of the target foil. Using in the above relation the kinetic energies of the emerging projectiles E_{out} given in Table II, the average equilibrium charge was found to be nearly the same for all targets, namely, 5.8+ for the C ions and 9.4+ for the Ne ions. Thus, in our investigations most of the projectiles interacting with the target atoms were either fully stripped ions or H-like ions. As a consequence, the EC process was not negligible and the observed $K\alpha$ diagram x-ray lines originated either from a single K -shell ionization or from a single capture of a K -shell electron, while the $K\alpha^h$ hypersatellite lines arose from a double K -shell ionization or a double K -shell electron capture or from the combination of a single K -shell ionization and a single K -shell electron capture.

The SCA model introduced by Bang and Hansteen [59] is an intermediate approach between classical physics and quantum mechanics in which the projectile is treated classically and the target atom using quantum theory. The SCA model is based on the first-order time-dependent perturbation theory. In this study, the modified SCA version of Trautmann and Rösel [38] using screened hydrogenlike wave functions (HWF) for the description of the target atom electrons was employed to calculate the single and double K -shell ionization cross sections. In the calculations performed within the separated-atom (SA) picture, the recoil of the target atom was considered and the projectile was assumed to have a pointlike charge distribution and to move along a classical hyperbolic trajectory.

TABLE IX. Reduced velocities η_K and rapidities ξ_K for the investigated collisions.

Target	η_K		ξ_K	
	C ions	Ne ions	C ions	Ne ions
Ca	1.21	0.91	2.88	2.50
V	0.89	0.68	2.42	2.12
Fe	0.69	0.53	2.10	1.84
Cu	0.56	0.43	1.86	1.63

TABLE X. Comparison between the double-to-single K -shell ionization cross-section ratios σ_{KK}/σ_K obtained in this work with the C ions and theoretical predictions from the SCA and CTMC models. All ratios are given in %. The SCA calculations were performed using hydrogenlike wave functions (HWF) and Dirac-Hartree-Fock wave functions (DHF). In the CTMC calculations the ratios were computed for the direct Coulomb ionization (DCI) only and for the DCI and electron capture (EC) contributions (DCI+EC). The theoretical cross-section ratios quoted in the last column were obtained using the SCA DHF model for the impact ionization cross sections and the CTMC calculations corrected by the scaling factor α for the electron capture cross sections. The cross sections were normalized beforehand to account for the effective charge of the projectiles. For details, see text. The ratios ω_K/ω_{KK} of the fluorescence yields for singly and doubly K -shell ionized atoms are also quoted.

Target	ω_K/ω_{KK}	σ_{KK}/σ_K					
		Present	SCA		CTMC		DCI(SCA DHF)+ α ×EC(CTMC)
			HWF	DHF	DCI	DCI+EC	
Ca	0.880	2.40(44)	1.47	1.78	3.27	4.74	2.01
V	0.934	1.77(33)	1.36	1.56	2.43	4.12	1.90
Fe	0.967	1.59(32)	1.19	1.35	2.06	3.60	1.71
Cu	0.950	1.35(26)	1.01	1.11	1.42	2.70	1.26

The corresponding cross-section ratios $(\sigma_{KK}/\sigma_K)_{SCA\ HWF}$ are quoted in the fourth columns of Tables X and XI.

In a more recent version of the SCA code, the radial hydrogenic wave functions were replaced by more realistic Dirac-Hartree-Fock wave functions (DHF) for both bound and continuum states [60]. As this change resulted into a much better agreement between experiment and theory for the ionization probabilities of the L shell [61] and especially the M shell [62], SCA DHF calculations were also carried out for this study. As shown in Tables X and XI, the double-to-single ionization cross-section ratios $(\sigma_{KK}/\sigma_K)_{SCA\ DHF}$ are bigger than the ones obtained with the SCA HWF calculations and closer to the experimental ratios. Actually, as the uncertainties on the experimental ratios are rather large (about 20%), the theoretical SCA DHF predictions are in agreement with the experimental values except for the C-Ca collision. However, for all collisions the ratios predicted by the SCA DHF model are systematically smaller than the experimental values.

As the above-mentioned deviations might be due to the fact that the EC process is not considered in the SCA model, the cross-section ratios were also calculated using classical trajectory Monte Carlo (CTMC) simulations [63–67] from which both the impact-induced ionization and electron capture cross sections can be obtained. For each collision, 500 000 particle trajectories were simulated. The calculations were performed within the frozen-atom picture. The charge of the atomic nucleus was calculated using the Slater recipe but the interaction between the two K -shell electrons was neglected. The collision trajectories were calculated for all processes creating a singly or doubly ionized $1s$ state of the target atoms,

namely, the impact-induced single K -shell ionization (SI), the single $1s$ target electron capture (SC), the impact-induced double K -shell ionization (DI), the double $1s$ target electron capture (DC), and the combination of an impact-induced single K -shell ionization and a single $1s$ target electron capture (SI+SC).

In the CTMC approach, the cross section is given by [64]

$$\sigma_r = \frac{N_r}{N} \pi b_{\max}^2, \tag{19}$$

where $r = \text{SI, SC, DI, DC, or SI+SC}$, N_r stands for the number of collisions satisfying the criteria for the process r , N is the total number of calculated trajectories, and b_{\max} the largest value of the impact parameter for which impact ionization or charge transfer can occur. For both the SCA and CTMC calculations, the cross sections were computed for three beam energies, namely, for 135, 140, and 145 MeV in the case of C and 170, 175, and 180 MeV in the case of Ne. The theoretical cross sections corresponding to the average beam energies quoted in Table II were then determined by linear interpolation.

The SI and DI cross sections provided by the CTMC calculations for the C-Ca collision are for instance 144 and 4.7 kb, respectively, whereas the SC, DC, and SI+SC cross sections amount to 71, 1.1, and 4.7 kb, respectively, indicating that the electron capture process is indeed not negligible for this collision. The SI and DI cross sections predicted for the same collision by the SCA HWF model are 120 and 1.8 kb, those obtained from the SCA DHF calculations 154 and 2.7 kb, respectively. One sees that the CTMC SI cross section is similar

TABLE XI. Same as Table X but for the collisions with the Ne ions.

Target	ω_K/ω_{KK}	σ_{KK}/σ_K					
		Present	SCA		CTMC		DCI(SCA DHF)+ α ×EC(CTMC)
			HWF	DHF	DCI	DCI+EC	
Ca	0.880	6.58(1.16)	4.99	5.79	5.41	10.63	6.34
V	0.934	4.96(94)	4.31	4.91	4.10	8.84	5.46
Fe	0.967	4.12(69)	3.57	3.95	2.86	6.55	4.41
Cu	0.950	3.55(69)	2.88	3.09	1.93	4.88	3.46

to the one provided by the SCA DHF model but the CTMC DCI cross section is almost 1.8 times bigger and thus probably overestimated. The same trend is also observed for the other targets and this explains why the CTMC DCI cross-section ratios quoted for the C ions in the sixth column of Table X are bigger than the SCA ones.

For the Ne-Ca collision, the CTMC cross sections are $\sigma_{\text{SI}} = 242$ kb, $\sigma_{\text{SC}} = 389$ kb, $\sigma_{\text{DI}} = 13$ kb, $\sigma_{\text{DC}} = 31$ kb, and $\sigma_{\text{SI+SC}} = 42$ kb. For comparison, the corresponding SI and DI cross sections predicted by the SCA HWF and SCA DHF models are 368 and 18 kb, and 455 and 26 kb, respectively. For the Ne-Ca collision, the SI and DI CTMC cross sections are thus smaller by a factor 1.9 for SI and 2.0 for DI than the SCA DHF ones, so that the CTMC DCI σ_{KK}/σ_K cross-section ratio is somewhat smaller (about 7%) than the SCA DHF one. For the collisions between Ne and the three other targets, the differences between the DI cross sections predicted by the CTMC and SCA DHF are more pronounced so that the CTMC DCI cross-section ratios are significantly smaller than the SCA DHF ones, the relative deviations increasing with Z from 20% for V up to 60% for Cu.

As mentioned before, the average equilibrium charge Z_{av} of the C beam in all four targets was found to be 5.8+. If one assumes that the percentage of ions with a charge smaller than $(Z - 1)$ was negligible, which is reasonable if one considers the variances of the ion charge distributions reported in Ref. [58], one can conclude that 80% of the C ions were fully stripped and 20% of them had still one $1s$ electron. As the calculations were performed for bare ions, the obtained DCI and EC cross sections should be corrected to account for the percentage of non-completely-stripped projectiles. In other words, as the DCI cross sections are proportional to the squared charge of the projectile, the SI and DI cross sections should be multiplied by $(5.8/6)^2 = 0.93$, the DC cross sections by 0.8, and the SC cross sections by $(0.8 \times 2 + 0.2 \times 1)/2 = 0.9$ since two $1s$ holes are available for 80% of the projectiles but only one for the remaining 20% C^{5+} ions. As a consequence, for the collisions with the C ions, the total cross sections including both the DCI and EC contributions were calculated using the following relations:

$$\sigma_K = 0.93 \times \sigma_{\text{SI}} + 0.90 \times \sigma_{\text{SC}}, \quad (20)$$

$$\sigma_{KK} = 0.93 \times \sigma_{\text{DI}} + 0.80 \times \sigma_{\text{DC}} + 0.84 \times \sigma_{\text{SI+SC}}. \quad (21)$$

Similarly, for Ne the average equilibrium charge was found to be 9.4+, which means that in this case only 40% of the ions were fully stripped and 60% of them corresponded to Ne^{9+} ions. Thus, for the Ne beam the SI and DI cross sections should be multiplied by 0.88, the DC cross sections by 0.4, and the SC cross sections by $(0.4 \times 2 + 0.6 \times 1)/2 = 0.7$. For the collisions with Ne, the total cross sections were thus calculated as follows:

$$\sigma_K = 0.88 \times \sigma_{\text{SI}} + 0.70 \times \sigma_{\text{SC}}, \quad (22)$$

$$\sigma_{KK} = 0.88 \times \sigma_{\text{DI}} + 0.40 \times \sigma_{\text{DC}} + 0.62 \times \sigma_{\text{SI+SC}}. \quad (23)$$

The CTMC cross-section ratios calculated using the above equations are presented in the seventh columns of Tables X and XI. From the comparison of the CTMC DCI cross-

section ratios which remain unchanged when Z_p is replaced by Z_{av} and the CTMC DCI+EC ones, one sees that, as assumed, the consideration of the EC process increases the cross-section ratios. Actually, the increase is too large since the CTMC DCI+EC cross-section ratios are clearly too big, about 2.2 times bigger than the experimental ones for C and 1.6 times bigger for Ne. This is, however, not really surprising because it is well known that the EC cross sections [56] are considerably overestimated by theory [68]. In order to take into consideration this overestimation of the theoretical EC cross sections, we have scaled the CTMC EC predictions, corrected beforehand for the effective charge of the ions, by multiplying them with a constant parameter α . The same value of α was assumed for the C and Ne ions. The scaling parameter α was determined by minimizing the sum of the squared differences between the experimental cross-section ratios σ_{KK}/σ_K and the scaled theoretical cross-section ratios, using the SCA DHF cross sections for the impact-induced single and double ionization and the CTMC cross sections for the single and double electron capture processes. A value $\alpha = 0.11$ was obtained. The theoretical σ_{KK}/σ_K cross-section ratios determined this way are presented in the eighth columns of Tables X and XI. As it can be seen, a quite satisfactory agreement with experiment is observed in this case, all ratios quoted in the third (experimental ratios) and eighth columns being consistent within the quoted experimental errors.

V. SUMMARY AND CONCLUDING REMARKS

We have investigated the radiative decay of double K -shell vacancy states produced in solid Ca, V, Fe, and Cu targets by impact with about 10 MeV/amu C and Ne ions. The K -hypersatellite x-ray lines were measured by means of high-energy-resolution spectroscopy using a von Hamos curved crystal spectrometer whose FWHM energy resolution varied between 1.6 eV for Ca and 3.4 eV for Cu. From the fits of the x-ray spectra corrected for the beam intensity, beam profile, and target self-absorption as well as for the variation with the energy of the solid angle of the spectrometer, effective size of the radiation source, crystal reflectivity and CCD efficiency, the energy shifts, linewidths, and relative intensities of the hypersatellite lines could be determined.

In general, the values obtained in this work for the energy shifts of the hypersatellites with respect to their parent diagram lines were found to be in satisfactory agreement with other existing experimental data and theoretical predictions. On the other hand, if one compares our values with the most recent and most precise hypersatellite energy shifts determined using synchrotron radiation, one finds that the average of the absolute values of the deviations amount to 0.9 eV for the $K\alpha_2^h$ hypersatellites and to 2.0 eV for the $K\alpha_1^h$ hypersatellites, whereas the averaged combined errors amount to 0.3 and 1.0 eV, respectively. In that sense, the two sets of energies are not consistent within the quoted $1 - \sigma$ errors. The main reason for this discrepancy resides probably in the fact that the shapes of the close-lying M satellites of the hypersatellites were not reproduced perfectly by the single or double Voigtians used in the fits to account for these unresolved satellite structures. One can thus conclude that the hypersatellite energy shifts obtained in this work are characterized by an accuracy of

1 eV for the $K\alpha_2$ hypersatellites and 2 eV for the weaker $K\alpha_1$ hypersatellites, which is quite satisfactory for x-ray spectroscopy measurements performed with heavy-ion beams.

In average, the hypersatellite linewidths obtained in our work overestimate the values determined from synchrotron radiation measurements by about 10%. This is again due to the flawed fits of the close-lying M satellites induced by the strong multiple ionization characterizing atomic collisions involving heavy ions. In measurements performed with synchrotron radiation, the M -satellite induced broadening is much less crucial because the additional M -shell ionization can be produced only by shake and knockout processes which are about two orders of magnitude weaker than the DCI and EC processes.

The main objective of this work was to determine the single-to-double K -shell ionization cross sections for the eight investigated collisions. The cross-section ratios were deduced from the corrected relative intensities of the hypersatellites. The results were found to be on one hand consistent with the theoretical predictions provided by the SCA model based on Dirac-Hartree-Fock wave functions but, on the other hand, systematically bigger than the latter. This was explained by the fact that the electron capture process which is not considered

in the SCA model plays an important role in the investigated collisions as shown by CTMC calculations and leads to bigger cross-section ratios. However, when the EC process is taken into consideration, the theoretical cross-section ratios become significantly bigger than the experimental ones because, as shown in the literature, the EC cross sections are strongly overestimated by theory. The difficulty was circumvented by correcting the EC contribution with a scaling factor α which was determined by a least-squares-fit method. Finally, using the SCA DHF model for the determination of the DCI cross sections and the CTMC predictions corrected by the scaling factor $\alpha = 0.11$ for the EC cross sections, a quite satisfactory agreement between theory and experiment was found for the σ_{KK}/σ_K cross-section ratios.

ACKNOWLEDGMENTS

The financial support of the Swiss National Science Foundation is acknowledged. One of us (K.T.) wishes to acknowledge the financial support of the National Research, Development and Innovation Office (NKFIH) via the Grant No. KH 126886.

-
- [1] W. Heisenberg, *Z. Phys.* **32**, 841 (1925).
 [2] G. Charpak, C. R. Hebd. Séances Acad. Sci. **237**, 243 (1953).
 [3] J. P. Briand, P. Chevallier, M. Tavernier, and J. P. Rozet, *Phys. Rev. Lett.* **27**, 777 (1971).
 [4] F. R. Hirsh Jr., *Rev. Mod. Phys.* **14**, 45 (1942).
 [5] J. P. Briand, P. Chevallier, and M. Tavernier, *J. Phys. Colloq.* **32**, C4-165 (1971).
 [6] T. Åberg and J. Utriainen, *Phys. Rev. Lett.* **22**, 1346 (1969).
 [7] T. Mukoyama and K. Taniguchi, *Phys. Rev. A* **36**, 693 (1987).
 [8] J. A. R. Samson, W. C. Stolte, Z.-X. He, J. N. Cutler, Y. Lu, and R. J. Bartlett, *Phys. Rev. A* **57**, 1906 (1998).
 [9] J. Hozzowska, A. K. Kheifets, J.-Cl. Dousse, M. Berset, I. Bray, W. Cao, K. Fennane, Y. Kayser, M. Kavčič, J. Szlachetko, and M. Szlachetko, *Phys. Rev. Lett.* **102**, 073006 (2009).
 [10] J. Hozzowska, J.-Cl. Dousse, W. Cao, K. Fennane, Y. Kayser, M. Szlachetko, J. Szlachetko, and M. Kavčič, *Phys. Rev. A* **82**, 063408 (2010).
 [11] O. Keski-Rahkonen, J. Saijonmaa, M. Suvanen, and A. Servomaa, *Phys. Scr.* **16**, 105 (1977).
 [12] E. Mikkola and J. Ahopelto, *Phys. Scr.* **27**, 297 (1983).
 [13] E. P. Kanter, R. W. Dunford, B. Krässig, and S. H. Southworth, *Phys. Rev. Lett.* **83**, 508 (1999).
 [14] M. Oura *et al.*, *J. Phys. B: At. Mol. Opt. Phys.* **35**, 3847 (2002).
 [15] S. Huotari *et al.*, *J. Electron Spectrosc. Relat. Phenom.* **137-140**, 293 (2004).
 [16] R. Diamant, S. Huotari, K. Hämäläinen, R. Sharon, C. C. Kao, and M. Deutsch, *Phys. Rev. A* **79**, 062511 (2009).
 [17] L. Young *et al.*, *Nature (London)* **466**, 56 (2010).
 [18] G. Doumy *et al.*, *Phys. Rev. Lett.* **106**, 083002 (2011).
 [19] B. Rudek *et al.*, *Nat. Photon.* **6**, 858 (2012).
 [20] K. Tamasaku *et al.*, *Phys. Rev. Lett.* **111**, 043001 (2013).
 [21] H. Yoneda *et al.*, *Nat. Commun.* **5**, 5080 (2014).
 [22] P. Richard, W. Hodge, and C. F. Moore, *Phys. Rev. Lett.* **29**, 393 (1972).
 [23] P. Richard, in *Atomic Inner-Shell Processes*, edited by B. Crasemann (Academic Press, New York, 1975), p. 73.
 [24] D. J. Nagel, A. R. Knudson, and P. G. Burkhalter, *J. Phys. B: At. Mol. Phys.* **8**, 2779 (1975).
 [25] Y. Awaya *et al.*, *Phys. Lett. A* **61**, 111 (1977).
 [26] J. Rzakiewicz *et al.*, *Phys. Lett. A* **264**, 186 (1999).
 [27] M. Kopal, M. Kavčič, M. Budnar, J.-Cl. Dousse, Y.-P. Maillard, O. Mauron, P.-A. Raboud, and K. Tökési, *Phys. Rev. A* **70**, 062720 (2004).
 [28] M. Czarnota *et al.*, *Eur. Phys. J. D* **57**, 321 (2010).
 [29] M. Czarnota, D. Banaś, M. Berset, D. Chmielewska, J.-Cl. Dousse, J. Hozzowska, Y.-P. Maillard, O. Mauron, M. Pajek, M. Polasik, P. A. Raboud, J. Rzakiewicz, K. Słabkowska, and Z. Sujkowski, *Phys. Rev. A* **88**, 052505 (2013).
 [30] M. Czarnota *et al.*, *Rad. Phys. Chem.* **68**, 121 (2003).
 [31] S. M. Kahn *et al.*, *Astron. Astrophys.* **365**, L312 (2001).
 [32] C. A. Back, J. Grun, C. Decker, L. J. Suter, J. Davis, O. L. Landen, R. Wallace, W. W. Hsing, J. M. Laming, U. Feldman, M. C. Miller, and C. Wuest, *Phys. Rev. Lett.* **87**, 275003 (2001).
 [33] J. Dunn, A. L. Osterheld, R. Shepherd, W. E. White, V. N. Shlyaptsev, and R. E. Stewart, *Phys. Rev. Lett.* **80**, 2825 (1998).
 [34] J. P. Briand *et al.*, *J. Phys. B: At. Mol. Phys.* **9**, 1055 (1976).
 [35] B. Boschung, J.-Cl. Dousse, B. Galley, C. Herren, J. Hozzowska, J. Kern, C. Rhême, Z. Halabuka, T. Ludziejewski, P. Rymuza, Z. Sujkowski, and M. Polasik, *Phys. Rev. A* **51**, 3650 (1995).
 [36] J. Hozzowska, J.-Cl. Dousse, J. Kern, and Ch. Rhême, *Nucl. Instrum. Methods Phys. Res. Sect. A* **376**, 129 (1996).
 [37] <http://www.srim.org/SRIM/SRIM2003.htm>.
 [38] D. Trautmann and F. Rösel, *Nucl. Instrum. Methods* **169**, 259 (1980).
 [39] <http://www.nist.gov/pml/data/xcom/>.
 [40] R. D. Deslattes *et al.*, *Rev. Mod. Phys.* **75**, 35 (2003).

- [41] J. L. Campbell and T. Papp, *At. Data Nucl. Data Tables* **77**, 1 (2001).
- [42] G. K. Wertheim, M. A. Butler, K. W. West, and D. N. E. Buchanan, *Rev. Sci. Instrum.* **45**, 1369 (1974).
- [43] J. H. Scofield, *At. Data Nucl. Data Tables* **14**, 121 (1974).
- [44] D. J. Bristow, J. S. Tse, and G. M. Bancroft, *Phys. Rev. A* **25**, 1 (1982).
- [45] M. Sanchez del Rio and R. J. Dejus, <http://www.esrf.eu/UsersAndScience/Experiments/TBS/SciSoft/xop2.3/>.
- [46] J. Szlachetko *et al.*, *Rev. Sci. Instrum.* **78**, 093102 (2007).
- [47] A. M. Costa, M. C. Martins, J. P. Santos, P. Indelicato, and F. Parente, *J. Phys. B: At. Mol. Opt. Phys.* **40**, 57 (2007).
- [48] A. M. Costa, M. C. Martins, J. P. Santos, F. Parente, and P. Indelicato, *J. Phys. B: At. Mol. Opt. Phys.* **39**, 2355 (2006).
- [49] M. Polasik, K. Słabkowska, J. Rzakiewicz, K. Koziol, J. Starosta, E. Wiatrowska-Koziol, J.-Cl. Dousse, and J. Hozowska, *Phys. Rev. Lett.* **107**, 073001 (2011).
- [50] G. P. Williams, Electron Binding Energies, X-Ray Data Booklet, Lawrence Berkeley National Laboratory (2009), <http://xdb.lbl.gov/>.
- [51] J. P. Mossé, P. Chevallier, and J. P. Briand, *Z. Phys. A* **322**, 207 (1985).
- [52] G. Goldsztejn, T. Marchenko, R. Püttner, L. Journel, R. Guillemin, S. Carniato, P. Selles, O. Travnikova, D. Céolin, A. F. Lago, R. Feifel, P. Lablanquie, M. N. Piancastelli, F. Penent, and M. Simon, *Phys. Rev. Lett.* **117**, 133001 (2016).
- [53] L. Natarajan, *Phys. Rev. A* **78**, 052505 (2008).
- [54] M. O. Krause, *J. Phys. Chem. Ref. Data* **8**, 307 (1979).
- [55] G. Basbas, W. Brandt, and R. Laubert, *Phys. Rev. A* **7**, 983 (1973).
- [56] J. R. Oppenheimer, *Phys. Rev.* **31**, 349 (1928).
- [57] V. S. Nikolaev and I. S. Dmitriev, *Phys. Lett. A* **28**, 277 (1968).
- [58] K. Shima, T. Mikumo, and H. Tawara, *At. Data Nucl. Data Tables* **34**, 357 (1986).
- [59] J. Bang and J. M. Hansteen, *Kgl. Danske Videnskab Selskab, Mat.-Fys. Medd.* **31**(13) (1959).
- [60] Z. Halabuka, W. Perger, and D. Trautmann, *Z. Phys. D* **29**, 151 (1994).
- [61] B. Boschung, M. W. Carlen, J.-Cl. Dousse, B. Galley, C. Herren, J. Hozowska, J. Kern, C. Rhême, T. Ludziejewski, P. Rymuza, Z. Sujkowski, and Z. Halabuka, *Phys. Rev. A* **52**, 3889 (1995).
- [62] C. Herren, B. Boschung, J.-Cl. Dousse, B. Galley, J. Hozowska, J. Kern, C. Rhême, M. Polasik, T. Ludziejewski, P. Rymuza, and Z. Sujkowski, *Phys. Rev. A* **57**, 235 (1998).
- [63] M. Karplus, R. N. Porter, and R. D. Sharma, *J. Chem. Phys.* **43**, 3259 (1965).
- [64] R. E. Olson and A. Salop, *Phys. Rev. A* **16**, 531 (1977).
- [65] K. Tökési and G. Hock, *J. Phys. B: At. Mol. Opt. Phys.* **29**, L119 (1996).
- [66] K. Tökési, *Nucl. Instrum. Methods Phys. Res. Sect. B* **233**, 266 (2005).
- [67] T. Mukoyama, Y. Nagashima, and K. Tokési, *Nucl. Instrum. Methods Phys. Res. Sect. B* **279**, 41 (2012).
- [68] F.T. Chan and J. Eichler, *Phys. Rev. Lett.* **42**, 58 (1979).